

# Prediction of Progressive Fatigue Damage and Failure Behavior of IM7/977-3 Composites using the Reduced-Order Multiple Space-Time Homogenization Approach

Journal Title  
XX(X):1-14  
©The Author(s) 2016  
Reprints and permission:  
sagepub.co.uk/journalsPermissions.nav  
DOI: 10.1177/ToBeAssigned  
www.sagepub.com/  


Michael J. Bogdanor<sup>1</sup> and Caglar Oskay<sup>1</sup>

## Abstract

This manuscript presents the blind prediction of fatigue life performance in three laminated carbon fiber reinforced polymer (CFRP) composite layups using a reduced-order space-time homogenization model. To bridge the spatial scales, the modeling approach relies on the Eigendeformation-based reduced order homogenization method (EHM). To bridge the time scales associated with a single load cycle and the overall life of the composite, a homogenization-based accelerated multiple-time-scale integrator with adaptive time stepping capability is employed. The proposed multiscale modeling approach was used to predict the evolution of composite stiffness and progressive damage accumulation as a function of loading cycles, as well as residual strength after fatigue in tension and compression, for three layups ( $[0,45,90,-45]_{2s}$ ,  $[30,60,90,-60,-30]_{2s}$ , and  $[60,0,-60]_{3s}$ ). Following blind prediction, the experimental data from the blind prediction specimens were employed to better understand the failure mechanisms and recalibrate the model. This study was performed as a part of the Air Force Research Laboratory's "Damage Tolerant Design Principles" (DTDP) Program.

Keywords: carbon fiber composites, multiscale modeling, homogenization, fatigue

## Introduction

Degradation of the properties of composites under fatigue loading is an important design limiter for aerospace and other structures. While FRP composites typically exhibit favorable fatigue life and performance, the complexity of the failure mechanisms and their interactions has so far limited the ability to predict failure consistently across multiple layups, materials, and structural configurations. It is clearly beneficial to achieve the ability to accurately model damage accumulation mechanisms under cyclic loading conditions with the view that such a capability could facilitate a modeling and simulation based design and certification paradigm. This manuscript reports the capabilities of the multiple space-time homogenization model - a progressive damage analysis approach based on multiscale principles applied in the length and time scales - in predicting the progressive damage and failure in CFRP composites subjected to cyclic loading. This study was performed as a part of the Air Force Research Laboratory's "Damage Tolerant Design Principles" (DTDP) Program summarized in this special issue.

Fatigue life prediction of composite materials has largely relied on the application of fracture mechanics concepts along with the Paris law (Paris and Erdogan 1963), which relates the growth rate of a fatigue crack to the stress intensity factor range experienced at a material point (see e.g., Russell and Street (1987); Spearing et al. (1992); Gamstedt and Ostlund (2001); Turon et al. (2006); Harper and Hallett (2010), among many others). Additional modeling approaches including Hashin and Rotem's macroscopic

failure criterion (Hashin and Rotem 1973), the characteristic damage state approach (Reifsnider and Talug 1980), modulus degradation (Lee and Hwang 2000), and the multi-criterion approach (Payan and Hochard 2002) have also been successfully applied to predict composite fatigue life. Life prediction models based on continuum damage mechanics (CDM) (Kachanov 2013; Lemaitre 2012) are an alternative approach, where the damage state of the composite is idealized using internal state variables, rather than the growth of a distinct crack. CDM has been applied at the scale of a lamina (Poursartip et al. 1986; Allen et al. 1987; Ladeveze and LeDantec 1992; Matzenmiller et al. 1995; Camanho et al. 2007) or the scale of composite constituents (Abdelal et al. 2002; Fish and Yu 2002; Crouch et al. 2013).

The fatigue behavior of composite structures is multiscale both in space and time. In addition to the multiple length scales associated with the hierarchical morphological structure of the composite (constituent, lamina, macroscopic structure), the disparity between the characteristic time period of a representative load spectrum (or a unit load cell) and the overall life of the structure introduces multiple time scales. Employing multiscale modeling principles to address

<sup>1</sup>Department of Civil and Environmental Engineering, Vanderbilt University, Nashville, TN 37235, USA

## Corresponding author:

Caglar Oskay, Address: VU Station B#351831, 2301 Vanderbilt Place, Nashville, TN 37235, United States

Email: caglar.oskay@vanderbilt.edu

multiple length scales has reached a level of maturity in the past few years (see e.g., [Terada and Kikuchi \(1995\)](#); [Miehe et al. \(1999\)](#); [Kouznetsova \(2002\)](#); [Fish \(2013\)](#); [Oskay and Fish \(2007\)](#); [Weinan and Engquist \(2003\)](#); [Hou and Wu \(1997\)](#); [Oskay \(2012\)](#)). Especially in conjunction with a form of model order reduction technique ([Aboudi 1982](#); [Dvorak 1992](#); [Moulinec and Suquet 1994](#); [Ghosh and Moorthy 1995](#); [Fish et al. 1997](#); [Oskay and Fish 2007](#); [Crouch and Oskay 2010](#)), a number of multiscale approaches have been proposed to study the behavior of composite materials ([Castañeda 1991](#); [Fish and Yu 2001](#); [Kouznetsova 2002](#); [Yvonnet and He 2007](#); [Pindera and Bednarczyk 1999](#); [Crouch et al. 2013](#); [Hernández et al. 2014](#); [Bogdanor and Oskay 2016](#)).

Multiscale principles have also been applied to address the disparate time scales in the fatigue life prediction problem. Perhaps the most commonly used and simplest multiple time scale approach is block cycle modeling ([Paas et al. 1993](#)). The block cycle approach poses damage evolution as an ordinary differential equation, the rate of which is computed numerically by solving the response of the system at selected time points within its lifetime subjected to characteristic load cycles. The intermediate response is interpolated or extrapolated from the responses resolved at these sparse time points. More computationally rigorous approaches including wavelet-based analysis ([Anahid et al. 2009](#)) and homogenization ([Oskay and Fish 2004a,b](#); [Fish and Yuan 2005](#)) have also been proposed. Recently, Oskay and coworkers ([Crouch et al. 2013](#); [Oskay 2015](#)) employed homogenization principles in both space and time to model the behavior of composites subjected to fatigue. The computational efficiency of this approach was further improved by orders of magnitude using accelerated time integrators ([Crouch and Oskay 2015](#)).

In this manuscript, the multiscale space-time homogenization approach is employed to predict the life and progressive damage accumulation in IM7/977-3 CFRP composite specimens subjected to tension-tension fatigue. The constituent material (i.e., fiber and matrix) parameters of the multiscale model were calibrated using a suite of static and fatigue calibration experiments. Blind predictions of progressive stiffness degradation as a function of load cycles, progressive damage accumulation within specimens, and residual tensile and compressive strength after fatigue were performed for three composite layups. Upon completion of the blind prediction phase, the experimental data for the blind prediction experiments were obtained and used to recalibrate the multiscale model. The predictions were performed within the timelines of the DTDP program. A separate manuscript in this special issue provides further details of the programmatic aspects, including the time line, of the DTDP program, as well as the experiments performed for model calibration and prediction.

## Reduced-order space-time homogenization model

Progressive damage accumulation in FRP composites is driven by failure mechanisms at the scale of the material constituents (i.e., fiber and matrix). Unfortunately, even for a coupon sized composite specimen, it is computationally

infeasible to resolve the constituents of the composite and evaluate its response in a single scale finite element analysis. Computational homogenization (CH) provides a rigorous mathematical framework to bridge the length scale of the microstructural heterogeneity and that of the structure without recourse to full scale resolution. By the CH approach, the governing equations are separated into coupled microscale and macroscale systems defined over the characteristic cell (i.e., unit cell or representative volume element) and the structural domain, respectively.

Figure 1 illustrates the multiple spatial and temporal scales of the laminated composite structure subjected to fatigue loading. The spatial domain of the composite structure is denoted as  $\Omega \in \mathbb{R}^3$ . The macroscale position coordinate is denoted as  $\mathbf{x}$ .  $\Omega$  is comprised of a heterogeneous periodic characteristic cell. The domain of the microscopic cell is denoted as  $\Theta$  and the corresponding microscale position coordinate is  $\mathbf{y} = \mathbf{x}/\zeta$ , with the scaling parameter,  $0 < \zeta \ll 1$ . An arbitrary response field,  $\varphi$ , is also subject to fluctuations in time due to the cyclic loading. In an analogous fashion to the multiple spatial scales, the macrochronological coordinate,  $t$ , parameterizing the macrotemporal scale and the microchronological coordinate,  $\tau$ , parameterizing the microtemporal scale are introduced such that  $\tau = t/\eta$ , where  $0 < \eta \ll 1$  is the temporal scaling parameter. In the CH approach, the multiple spatial and temporal scales are employed along with a perturbation analysis to decompose the original equations (equilibrium, kinematic, and constitutive equations, as well as boundary conditions) governing the progressive failure within the structure into four coupled boundary value problems ([Crouch et al. 2013](#)). While this procedure provides a rigorous coupled system for fatigue life prediction it remains to be computationally expensive for analysis of realistic sized structures.

In order to increase the computational efficiency of the CH method, the Eigendefinition-based reduced order homogenization (EHM) method is employed. The theory, formulation, and computational aspects of the EHM method are provided in ([Oskay and Fish 2007](#); [Crouch and Oskay 2010](#)), and a very brief description of the theory is discussed herein. In the EHM approach, the domain of the characteristic cell,  $\Theta$ , is decomposed into  $n$  non-overlapping subdomains (i.e., parts) denoted as  $\theta^{(\gamma)}$ ,  $\gamma = 1, \dots, n$ . The number of parts is taken to be much smaller than the number of elements used to discretize the characteristic cell. The inelastic response fields are taken to be spatially constant within each part. Following the generalization of the transformation field theory ([Dvorak 1992](#)), microscale equilibrium is enforced through numerical approximations to influence functions defined over the characteristic cell. By this approach, the evaluation of the microscale problem reduces to the computation of the inelastic strain coefficients for each part, the number of which is proportional to the number of parts used in the model order reduction.

The multitemporal approach employed herein is a fast time-integration scheme as presented in [Crouch et al. \(2013\)](#) and [Crouch and Oskay \(2015\)](#). In microtime, damage evolves in the constituent materials due to the fast oscillations of the loading cycle. In macrotime, the accumulation of damage over multiple loading cycles leads to a redistribution of stress within the component. In order to upscale the

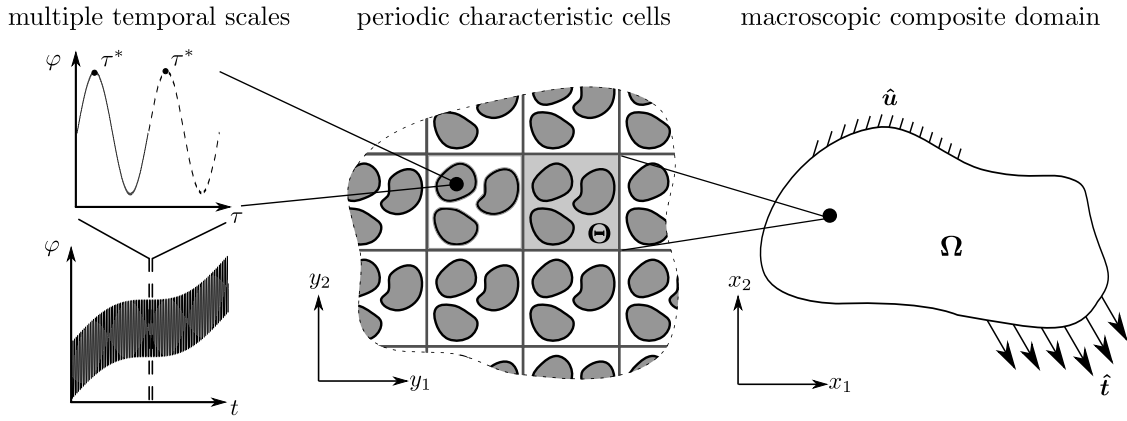


**Figure 1.** Multiple length and time scales.

microtemporal response to the macrotemporal scale, a temporal homogenization operator is employed. While in the context of multiple scales in space a spatial averaging operator is typically used, it is computationally more convenient to employ the fixed point operator for temporal homogenization (Crouch et al. 2013). In this approach, an arbitrary but fixed point,  $\tau^*$ , in the microchronological cycle is tracked during the macrochronological analysis.

Due to the irreversibility of damage evolution over a single step, the traditional concept of periodicity used in multispatial homogenization is not directly applicable to the temporal homogenization. Considering the change in damage at a material point over a microchronological cycle is small but non-zero, the response fields over the component are “almost-periodic” with respect to the homologous microtemporal point on successive load cycles. An almost periodic rate operator that accounts for the progressive accumulation of damage within the load cycles is considered to evolve the response fields over the macrochronological time (Oskay and Fish 2004a).

The multiscale system described above relies on calculating the response of the composite structure subjected to select characteristic load cycles during its lifetime. For large structural systems under high cycle fatigue conditions, evaluation of even a small number of such nonlinear problems may be computationally infeasible. The need to resolve each individual load cycle is eliminated by introducing a fast time integrator with adaptive macrochronological time stepping (Crouch et al. 2013). In this approach, the evolution of the damage state within a single load cycle is assumed to alter the equilibrium state of the structure an insignificant amount, decoupling damage evolution from equilibrium computations, and rendering the equilibrium within a load cycle a linear problem. The resulting system of coupled multispatial/multitemporal boundary value problems are as follows:

**Microchronological problem:** The microchronological equilibrium, kinematic relationship, and boundary conditions over the macrospatial domain,  $\Omega$ , are given as:

$$\nabla \cdot \bar{\boldsymbol{\sigma}}(\mathbf{x}, \tau, t) + \bar{\mathbf{b}}(\mathbf{x}) = 0; \quad \mathbf{x} \in \Omega; \quad \tau \in [0, \tau_0] \quad (1)$$

$$\bar{\boldsymbol{\epsilon}}(\mathbf{x}, \tau, t) = \nabla^s \bar{\mathbf{u}}(\mathbf{x}, \tau, t) \quad (2)$$

$$\bar{\mathbf{u}} = \hat{\mathbf{u}}(\mathbf{x}, \tau, t); \quad \mathbf{x} \in \Gamma_u \quad (3)$$

$$\bar{\boldsymbol{\sigma}} \cdot \mathbf{n} = \hat{\mathbf{t}}(\mathbf{x}, \tau, t); \quad \mathbf{x} \in \Gamma_t \quad (4)$$

where  $\bar{\boldsymbol{\sigma}}$  denotes the spatially homogenized macroscale stress,  $\bar{\mathbf{b}}$  the body force,  $\bar{\boldsymbol{\epsilon}}$  the homogenized macroscale strain,  $\bar{\mathbf{u}}$  the macroscale displacement, and  $\mathbf{n}$  the unit normal to the boundary. The structure is subjected to prescribed boundary displacements,  $\hat{\mathbf{u}}$ , within a subdomain of the boundary, whereas on the remainder of the boundary prescribed tractions,  $\hat{\mathbf{t}}$ , are applied.  $\nabla \cdot$  and  $\nabla^s$  indicate the divergence and symmetric gradient operators, respectively.

In this manuscript, the constitutive behavior of the composite constituents is idealized using a scalar continuum damage mechanics model further described below. The constitutive relationship between the homogenized macroscale stress and strain is derived through EHM. The inelastic strain coefficients,  $\boldsymbol{\mu}^{(\gamma)}$ , induced by the scalar damage coefficients,  $\omega^{(\gamma)}$ , in each part are computed as the solution to the following system of equations (Crouch and Oskay 2015):

$$\sum_{\Delta=1}^n \left\{ \left[ 1 - \omega^{(\Delta)}(\tau^*, t) \right] \left[ \hat{\mathbf{A}}^{(\alpha\Delta)} : \bar{\boldsymbol{\epsilon}}(\tau, t) + \dots \right. \right. \\ \left. \left. \sum_{\gamma=1}^n \hat{\mathbf{B}}^{(\alpha\Delta\gamma)} : \boldsymbol{\mu}^{(\gamma)}(\tau, t) \right] \right\} = 0 \quad \forall \alpha = 1, 2, \dots, n \quad (5)$$

where  $\hat{\mathbf{A}}$  and  $\hat{\mathbf{B}}$  are coefficient tensors computed as a function of the microstructural morphology and elastic constituent properties.

The homogenized macroscale stress,  $\bar{\boldsymbol{\sigma}}$ , is computed as a function of the inelastic strain and damage coefficients as:

$$\bar{\boldsymbol{\sigma}}(\tau, t) = \sum_{\Delta=1}^n \left[ 1 - \omega^{(\Delta)}(\tau^*, t) \right] \left[ \bar{\mathbf{L}}^{(\Delta)} : \bar{\boldsymbol{\epsilon}}(\tau, t) + \dots \right. \\ \left. \sum_{\alpha=1}^n \bar{\mathbf{P}}^{(\alpha\Delta)} : \boldsymbol{\mu}^{(\alpha)}(\tau, t) \right] \quad (6)$$

where  $\bar{\mathbf{L}}$  and  $\bar{\mathbf{P}}$  are coefficient tensors and  $\tau^*$  is the fixed point typically taken to be the initial state of a load cycle (i.e.,  $\tau^* = 0$ ). The form of the evolution equations for damage variables within each part is provided below.

**Macrochronological problem:** Over macrotime, the equilibrium equation, kinematic relationship, and boundary conditions are given as:

$$\nabla \cdot \bar{\boldsymbol{\sigma}}(\mathbf{x}, t) + \bar{\mathbf{b}}(\mathbf{x}) = 0; \quad \mathbf{x} \in \Omega; \quad t \in [0, t_f] \quad (7)$$

$$\tilde{\boldsymbol{\epsilon}}(\mathbf{x}, t) = \nabla^s \tilde{\mathbf{u}}(\mathbf{x}, t) \quad (8)$$

$$\tilde{\mathbf{u}} = \hat{\mathbf{u}}^0(\mathbf{x}, t); \quad \mathbf{x} \in \Gamma_{\mathbf{u}} \quad (9)$$

$$\tilde{\boldsymbol{\sigma}} \cdot \mathbf{n} = \hat{\mathbf{t}}^0(\mathbf{x}, t); \quad \mathbf{x} \in \Gamma_t \quad (10)$$

In the macrochronological problem, the response is homogenized in both space and time. The difference between Equations 7-10 for the macrochronological problem and Equations 1-4 for the microchronological problem is the presence of the fixed point operator,  $(\cdot)$ . The macrochronological displacement and traction boundary conditions, defined at  $\tau^*$ , are denoted as  $\hat{\mathbf{u}}^0$  and  $\hat{\mathbf{t}}^0$ , respectively. Using the almost periodicity idea, the rate of damage evolution within each part with respect to macrotime is given as:

$$\dot{\tilde{\omega}}_{,t}^{(\gamma)}(t) = f^1(\tilde{\boldsymbol{\epsilon}}(t)^{(\gamma)}, \tilde{\mathbf{s}}^{(\gamma)}(t); \boldsymbol{\Psi}^{(\gamma)}) + \dot{\omega}_{\text{ap}}^{(\gamma)}(t) \quad (11)$$

where  $f^1$  is the functional form of damage evolution with respect to macrotime,  $\tilde{\mathbf{s}}^{(\gamma)}$  denotes internal state variables,  $\boldsymbol{\Psi}^{(\gamma)}$  are the set of material parameters defining the evolution of damage, and  $\dot{\omega}_{\text{ap}} := \int_0^{\tau_0} (d\omega/d\tau) d\tau/\eta$  is the rate of almost periodic damage evolution from the microchronological solution of a single loading cycle. The temporally homogenized inelastic strain coefficients and temporally homogenized damage coefficients satisfy the following system of equations:

$$\sum_{\Delta=1}^n \left\{ \left[ 1 - \tilde{\omega}^{(\Delta)}(t) \right] \left[ \hat{\mathbf{A}}^{(\alpha\Delta)} : \tilde{\boldsymbol{\epsilon}}(t) + \dots \right. \right. \\ \left. \left. \sum_{\gamma=1}^n \hat{\mathbf{B}}^{(\alpha\Delta\gamma)} : \tilde{\boldsymbol{\mu}}^{(\gamma)}(t) \right] \right\} = 0 \quad \forall \alpha = 1, 2, \dots, n \quad (12)$$

and the temporally homogenized macroscale stress is computed as:

$$\tilde{\boldsymbol{\sigma}}(t) = \sum_{\Delta=1}^n \left[ 1 - \tilde{\omega}^{(\Delta)}(t) \right] \left[ \bar{\mathbf{L}}^{(\Delta)} : \tilde{\boldsymbol{\epsilon}}(t) + \dots \right. \\ \left. \sum_{\alpha=1}^n \bar{\mathbf{P}}^{(\alpha\Delta)} : \tilde{\boldsymbol{\mu}}^{(\alpha)}(t) \right] \quad (13)$$

### Damage evolution equations

A cycle-sensitive, isotropic continuum damage mechanics model is employed to characterize progressive damage evolution in the composite constituents (Oskay and Fish 2004a; Fish and Yu 2002). The rate of damage evolution within part  $\gamma$  of the reduced order model (ROM) is expressed as:

$$\dot{\omega}^{(\gamma)} = g^p \frac{d\Phi(v^{(\gamma)})}{dv^{(\gamma)}} \langle \dot{v}^{(\gamma)} \rangle_+,$$

$$\text{where } 0 \leq g = \frac{\Phi(v^{(\gamma)})}{\omega^{(\gamma)}} \leq 1; \quad \gamma = 1, 2, \dots, n \quad (14)$$

in which the superimposed dot indicates the time derivative,  $p$  models cyclic damage sensitivity, and  $\langle \cdot \rangle_+$  indicates Macaulay brackets ( $\langle \cdot \rangle_+ = [(\cdot) + |\cdot|]/2$ ). Damage evolution within each constituent part is driven by the damage equivalent strain,  $v^{(\gamma)}$ :

$$v^{(\gamma)} = \sqrt{\frac{1}{2} (\mathbf{F}^{(\gamma)} \boldsymbol{\epsilon}^{(\gamma)}) : \hat{\mathbf{L}}^{(\gamma)} : (\mathbf{F}^{(\gamma)} \boldsymbol{\epsilon}^{(\gamma)})} \quad (15)$$

where  $\boldsymbol{\epsilon}^{(\gamma)}$  denotes the principal strain vector,  $\hat{\mathbf{L}}^{(\gamma)}$  the elastic moduli tensor for the constituent material in part  $\gamma$  rotated to the direction of the principal strains, and  $\mathbf{F}^{(\gamma)}$  is the strain weighting matrix for tension/compression damage anisotropy:

$$\mathbf{F}^{(\gamma)} = \begin{bmatrix} h_1 & 0 & 0 \\ 0 & h_2 & 0 \\ 0 & 0 & h_3 \end{bmatrix} \quad (16)$$

$$h_\xi = \begin{cases} 1 & \text{if } \hat{\epsilon}_\xi > 0 \\ c^{(\gamma)} & \text{otherwise} \end{cases} \quad \text{for } \xi = 1, 2, 3 \quad (17)$$

in which  $c^{(\gamma)}$  is the tension/compression anisotropy factor for part  $\gamma$ .

$\Phi$  is the damage potential function:

$$\Phi(v^{(\gamma)}) = \frac{\arctan(a^{(\gamma)} \langle v^{(\gamma)} - v_0^{(\gamma)} \rangle_+ - b^{(\gamma)}) + \arctan(b^{(\gamma)})}{\frac{\pi}{2} + \arctan(b^{(\gamma)})} \quad (18)$$

in which  $a^{(\gamma)}$ ,  $b^{(\gamma)}$ , and  $v_0^{(\gamma)}$  are material parameters which control the shape (e.g., magnitude, ductility, threshold) of damage evolution. The ductility control variable,  $b^{(\gamma)}$ , is weighted to model the ductile matrix behavior under shear dominated loading as well as the brittle matrix behavior under normal dominated loading conditions:

$$b^{(\gamma)} = k_b b_s^{(\gamma)} + (1 - k_b) b_n^{(\gamma)} \quad (19)$$

$$k_b = \frac{\gamma_{\text{max}}^{(\gamma)}}{\gamma_{\text{max}}^{(\gamma)}/2 + \epsilon_{\text{max}}^{(\gamma)}}; \quad \in [0, 1] \quad (20)$$

where,  $b_s^{(\gamma)}$  is the shear ductility parameter,  $b_n^{(\gamma)}$  the normal ductility parameter,  $k_b$  the local loading dependent weighting parameter,  $\gamma_{\text{max}}^{(\gamma)}$  the maximum shear strain in part  $\gamma$ , and  $\epsilon_{\text{max}}^{(\gamma)}$  the part maximum absolute principal strain. This disparity in material behavior from loading modes is not observed in the fiber material, therefore no weighting is considered for the fiber ductility parameter and single parameter,  $b^{(f)}$ , is implemented for the fiber.

The fatigue life of both the fiber and matrix materials is dependent on the amplitude of stress experienced in the cyclic loading. The cyclic damage sensitivity,  $p$ , is computed as:

$$p^{(\gamma)} = d_0^{(\gamma)} + d_1^{(\gamma)} v_{\text{max}}^{(\gamma)} + d_2^{(\gamma)} (v_{\text{max}}^{(\gamma)})^2 \quad (21)$$

where  $d_0^{(\gamma)}$ ,  $d_1^{(\gamma)}$ , and  $d_2^{(\gamma)}$  are material parameters and  $v_{\text{max}}^{(\gamma)}$  is the largest damage equivalent strain value in the part  $\gamma$  experienced over the entire loading history,

$$v_{\text{max}}^{(\gamma)}(t) = \max_{s \in [0, t]} \{v^{(\gamma)}(s)\} \quad (22)$$

### Form of the reduced order model

The four part ROM employed in this study to represent the partitioning of the microstructural unit cell is shown in Figure 2. Part 1 consists of the fiber material and parts 2-4 are composed of the matrix. Damage in part 1 indicates the presence of fiber failure, part 2 the growth of transverse matrix cracking, part 3 interply delamination, and part 4 represents the intersection of the delamination and transverse matrix cracking failure modes.

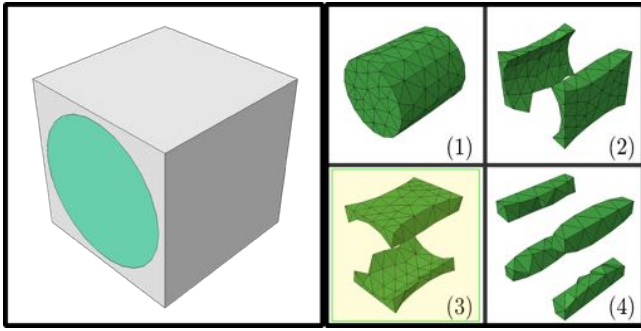


**Figure 2.** Parts of the reduced order model.

In the blind prediction phase, parts 2-4, which constitute the matrix domain, are assigned the same set of material parameters:  $\Psi^{(m)} = \{a^{(m)}, b_n^{(m)}, b_s^{(m)}, c^{(m)}, v_0^{(m)}, d_0^{(m)}, d_1^{(m)}, d_2^{(m)}\}$ . The behavior within part 1 that constitutes the fiber material is described by the set of parameters  $\Psi^{(f)} = \{a^{(f)}, b^{(f)}, c^{(f)}, v_0^{(f)}, d_0^{(f)}, d_1^{(f)}, d_2^{(f)}\}$ . In recalibration, part 3, which idealizes delamination failure, was recalibrated using a separate material parameter set to better capture interlaminar failure in both static and fatigue loading. The delamination part parameters are denoted as  $\Psi^{(d)}$ . The calibration and recalibration of  $\Psi^{(m)}$ ,  $\Psi^{(f)}$ , and  $\Psi^{(d)}$  are described in a later section.

## Implementation

Figure 3 illustrates the implementation strategy for the coupled microchronological and macrochronological problems that constitute the reduced order space-time homogenization model. The two time-scale problems are evaluated using the commercial finite element package, Abaqus. A driver script written in the Python programming language controls the execution of the approach and transfers information between the coupled problems. Prior to the progressive failure analysis (i.e. pre-processing), the microstructural geometry of the composite along with the elastic properties of the constituents are used to generate the EHM coefficients. Input files are constructed using the EHM coefficients, constituent failure parameters defining the material response, and the macroscale geometry, layup, and boundary and loading conditions. The driver script then uses the input files to perform the multitemporal analyses: in turn evaluating the response to a single microchronological load cycle to determine the almost periodic rate of damage evolution and solving a step of the macrochronological problem. An adaptive macrochronological time stepping strategy is employed, where the driver script computes the macrotime step based on the damage rates computed within the microchronological problem (Crouch et al. 2013; Crouch and Oskay 2015). The procedure is repeated until specimen failure or when the specified maximum number of load cycles is reached. Python scripting was also used to obtain the stress and strain response of the specimens at each resolved step and to produce the damage contour plots to demonstrate progressive damage accumulation patterns as analysis output.

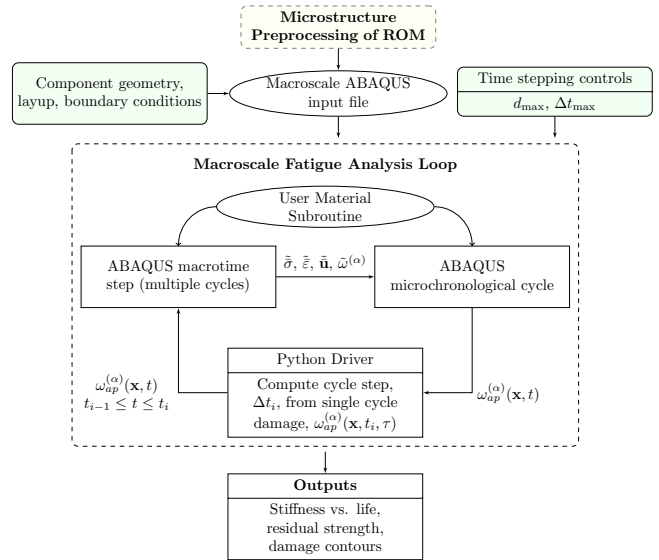


**Figure 3.** Computational implementation of the multiple space-time homogenization model for fatigue failure prediction.

## Calibration, blind prediction and recalibration procedure

The fatigue prediction exercise performed as a part of the DTDP program and described below followed a similar prediction study outlined in Bogdanor and Oskay (2016). First, a suite of calibration experiments performed on simple layups were used to calibrate the model parameters. The calibrated model was then employed to perform blind predictions of specimen stiffness degradation and damage evolution as a function of load cycles, as well as residual strength after fatigue of three composite layups. Following blind predictions the experimental data pertaining to the blind prediction phases were received and the model was recalibrated. The calibration, blind prediction, and recalibration procedures are described below. Further details on the specific experiments used in the DTDP program are provided in a separate publication within this special issue.

### Calibration

Eight model parameters ( $a^{(m)}, b_n^{(m)}, b_s^{(m)}, c^{(m)}, v_0^{(m)}, d_0^{(m)}, d_1^{(m)}$ , and  $d_2^{(m)}$ ) that define damage evolution in the matrix and seven parameters ( $a^{(f)}, b^{(f)}, c^{(f)}, v_0^{(f)}, d_0^{(f)}, d_1^{(f)}$ , and  $d_2^{(f)}$ ) that define the failure of the fiber were calibrated for the blind prediction model. The calibrated values for these parameters are presented in Table 1 (Columns 2 and 3). An additional column (Column 4) is included in Table 1 showing the calibrated parameters of the delamination part which were included in the recalibration phase described below. Out of the two parameter sets (i.e., matrix and fiber) five parameters of the matrix set and four parameters of the fiber set describe the static failure behavior. These parameters were calibrated using experimental data for the static prediction study described in detail in Bogdanor and Oskay (2016). In what follows, the calibration of the parameters describing the cycle sensitivity of the damage evolution law are presented. The parameters controlling the cycle-sensitivity parameter are  $d_0$ ,  $d_1$ , and  $d_2$  for each constituent.

**Table 1.** Calibrated material damage evolution parameters.

Property	Fiber	Matrix	Delamination
$a$	0.050562	0.001592	0.018
$b_n$	274	15	304.0
$b_s$	-	-3.2	9.45
$c$	1.4481	0.535	0.492
$\nu_0$	1367	636.2	0
$d_0$	10.735	6.0	6.0
$d_1$	$-2.07E-3$	$-3.0E-3$	$-6.0E-3$
$d_2$	$-1.04E-10$	$-2.62E-10$	$-2.62E-10$

The stress-life curves obtained from the  $90^\circ$  three point bending fatigue experiments were used to calibrate the matrix cycle sensitivity parameters ( $d_0^{(m)}$ ,  $d_1^{(m)}$ , and  $d_2^{(m)}$ ). Similarly, the stress-life curves of the  $0^\circ$  tension-tension fatigue experiments were used to calibrate the fiber parameters ( $d_0^{(f)}$ ,  $d_1^{(f)}$ , and  $d_2^{(f)}$ ). In both cases the optimization was performed using the Nelder-Mead simplex method (Nelder and Mead 1965) to minimize the discrete  $L_2$  norm of the differences between the best power law fit to the experimental data for cycles to failure and the simulated cycles to failure. The calibrations employed data from  $90^\circ$  three-point bend tests with 19 samples subjected to loading amplitudes between 55% and 75% of the mean static ultimate strength of 130 MPa, and  $0^\circ$  unidirectional tests with 13 samples subjected to loading amplitudes between 77% and 90% of the mean static ultimate strength of 2855 MPa. All fatigue tests were performed with an R-ratio of 0.1. The resulting calibrated stress-life curves are shown in Figure 4. The calibration method was able to generate a model which very closely matches the power law fit for the calibration experiments. It is noted that there is a significant amount of variability in the experimental fatigue life of the  $90^\circ$  specimens. This variability represents a significant source of uncertainty in the prediction of the fatigue life of laminates. The present study is focused on demonstrating the deterministic predictive capability of the EHM model, however Bayesian statistical methods have been employed within the EHM framework in previous investigations to predict laminate behavior under model parameter uncertainty (Bogdanor et al. 2013, 2015).

### Blind Prediction

The calibrated model was exercised to predict the stiffness degradation, progressive damage accumulation, and residual strength after fatigue in tension and compression for the  $[0,45,90,-45]_{2s}$ ,  $[30,60,90,-60,-30]_{2s}$ , and  $[60,0,-60]_{3s}$  specimens with open-hole configurations under tension-tension fatigue. Each of the specimens were 38.1 mm wide with a gage section length of 138 mm. The open hole in each case was 6.35 mm in diameter, centered on the specimen in both the width and length dimensions. The thickness of the  $[0,45,90,-45]_{2s}$  specimen was 2.0 mm, the  $[30,60,90,-60,-30]_{2s}$  specimen was 2.5mm, and the  $[60,0,-60]_{3s}$  specimen 2.25 mm. For all specimens, the finite element mesh lines in the discretization of each ply were oriented parallel to the direction of the fiber to align the mesh direction with the general direction of failure to alleviate the effect of mesh bias, which refers to the propensity of failure to propagate along mesh lines. The finite element

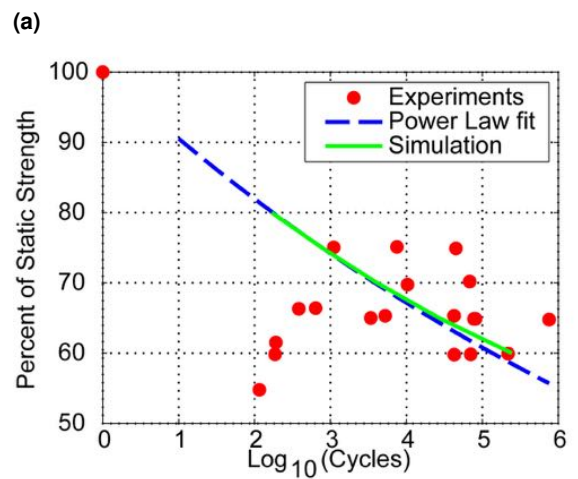
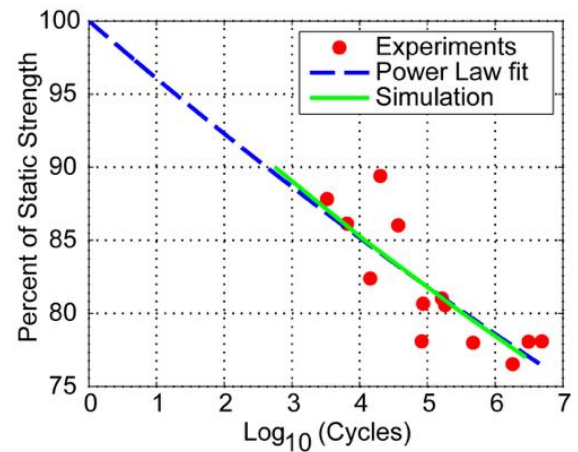


**Figure 4.** Fatigue stress vs. life curves for (a)  $0^\circ$  tension-tension fatigue and (b)  $90^\circ$  three point bending fatigue.

mesh consisted of elements with out-of-plane dimension equal to one ply thickness (0.125mm) and a nominal edge length in the in-plane directions of  $h = 1\text{mm}$  to maintain consistent element sizes throughout the specimens. The surfaces of adjacent plies were connected using surface tie constraints since the meshes of neighboring plies are not necessarily compatible. Further details of the macroscale mesh and layups are included in Bogdanor and Oskay (2016). In the cyclic analysis, a pinned boundary was applied at one end of the specimen constraining displacement in the coupon longitudinal direction and a uniform, monotonically increasing displacement was applied to the opposite end such that the average stress over the gross cross section of the coupon was equal to the applied stress level. For the prediction of residual strength after fatigue, the numerical specimens were subjected to a fixed number of load cycles as described above and unloaded. An additional analysis step was then performed where the fatigued specimens were monotonically loaded to failure under tension or compression with the damage state computed in the cyclic loading steps as the initial condition.

The numerical analyses were performed using a parallel computing cluster with 16 2.1GHz AMD Opteron(TM) 6272 Processors and 128 GB shared memory on each compute node. In blind predictions, each of the analyses

were performed using 40 processors in a distributed memory configuration. The number of elements and nodes in the finite element mesh, number of resolved cycles, and wall time for each of the three prediction cases are shown in Table 2. It is noted that the  $[0,45,90,-45]_{2s}$  and  $[30,60,90,-60,-30]_{2s}$  specimens both reached 2 million cycles without structural failure, while the  $[60,0,-60]_{3s}$  specimen exhibited significantly premature failure in the blind predictions.

**Table 2.** Numerical specimen mesh size and wall time for failure analysis.

Layup	No. of elements	No. of nodes	Resolved cycles	Wall time (H:MM)
$[0, 45, 90, -45]_{2s}$	29,264	61,216	192	33:48
$[30, 60, 90, -60, -30]_{2s}$	40,498	84,412	175	89:26
$[60, 0, -60]_{3s}$	37,131	77,370	17	3:16

### Recalibration

As further discussed below, a discrepancy in the stiffness degradation rates for the  $[60,0,-60]_{3s}$  specimen was observed between the predictions of the model and the experimental results. Starting from the hypothesis that the interlaminar shear and consequent delamination behavior is not adequately captured by the blind prediction model, the recalibration phase of the study focused on the investigation of how the interlaminar shear behavior could be better captured. In order to recalibrate the model for interlaminar shear, the experimental data from the end notch flexure (ENF) experiments were utilized. These experiments were performed at the AFRL as a part of the DTDP program and already provided as initial calibration data. These experiments were not used in the original calibration of the model.

For consistency of blind predictions, ENF experiments under static and fatigue loading were employed in the recalibration. Upon recalibration, all static prediction cases (not reported in this manuscript, but reported in Bogdanor and Oskay (2016)) were simulated again and the accuracy of the predictions relative to the static blind predictions and recalibrations were confirmed. The material parameters in part 3 of the ROM were calibrated to match the ENF static and fatigue experiments, as shown in Figure 5. The recalibrated material parameters are reported in Table 1 (Column 4). Additionally, the  $0^\circ$  plies in the  $[60,0,-60]_{3s}$  were modeled with 3 elements per ply thickness to better capture interlaminar stress states. The change in the parameter values describing matrix failure in part 3 of the ROM and the additional mesh refinement in the through-thickness direction of the  $0^\circ$  plies were the only modeling changes applied in the recalibrated model. While the modeling changes in recalibration was driven by the results of  $[60,0,-60]_{3s}$  layup, the same recalibrated model (parameter values, meshing strategy, multitemporal controls) was used consistently across the  $[0,45,90,-45]_{2s}$ ,  $[60,0,-60]_{3s}$ , and  $[30,60,90,-60,-30]_{2s}$  layups.

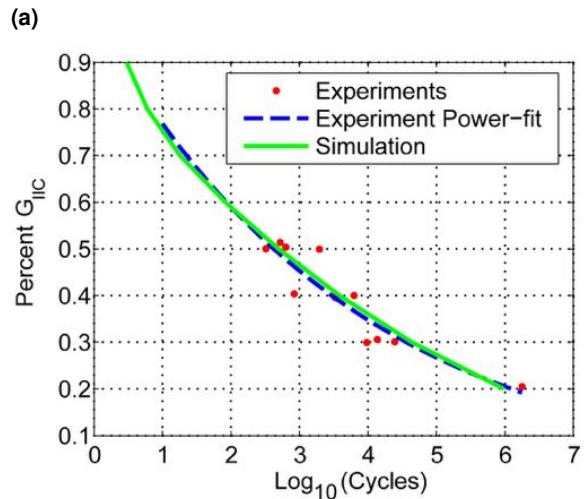
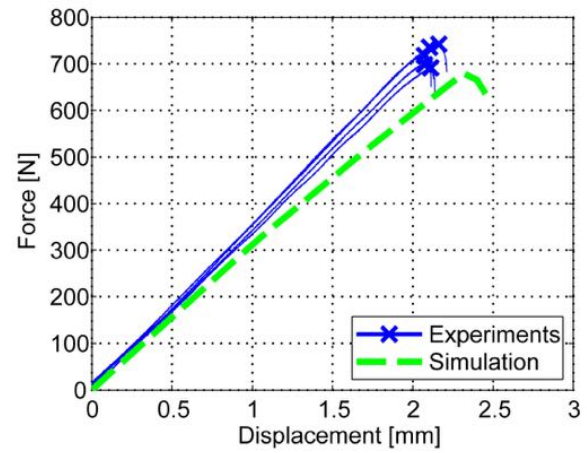


**Figure 5.** Calibrated model comparisons with ENF tests for (a) stress vs. strain in static loading and (b) critical energy vs. life in fatigue.

## Results and Discussion

### Stiffness vs. Cycles under Fatigue

The three composite specimens were subjected to tension-tension fatigue loading with an R-ratio of 0.1 up to 2 million cycles (i.e., runout) or failure. The applied loading was 50% of the static ultimate strength of the  $[0,45,90,-45]_{2s}$  layup, 40% of the  $[30,60,90,-60,-30]_{2s}$  layup and, 80% of the  $[60,0,-60]_{3s}$  layup. The stress in a given specimen was computed as the sum of the reaction forces at the pulled end of the specimen divided by the gross cross-sectional area of the specimen. Strain was computed as the change in relative displacement on two nodes in the finite element mesh of the exterior ply 1/2 inch above and 1/2 inch below the center of the open hole centered on the specimen, divided by the initial distance between the points of 1 inch. This strain measure was used to represent the behavior of the extensometer employed in the experimental set up. In blind predictions and after recalibration, the stiffness degradation behavior of the  $[0,45,90,-45]_{2s}$  and  $[30,60,90,-60,-30]_{2s}$  layups as predicted by the model were in reasonably good agreement with the experiments. The stiffness degradation as a function of number of load cycles for the  $[0,45,90,-45]_{2s}$  layup compared with the individual

experiment data (Figure 6) shows that the simulation predicts the initial stiffness drop over the first few thousand cycles and the following plateau. The simulation did not predict failure in the specimen. In the experiments, many of the specimens did fail, but over a wide range of cycles (from approximately 400K cycles to 1.65M cycles). The stiffness degradation curves for the  $[30,60,90,-60,-30]_{2s}$  as observed in the experiments and simulations are shown in Figure 7. The simulation results are largely in good agreement with the experiments for the  $[30,60,90,-60,-30]_{2s}$  layup. In this case, neither the experiments nor the simulation demonstrated specimen failure. The recalibration of the model had only minor effects on the stiffness degradation behavior for the  $[0,45,90,-45]_{2s}$  and  $[30,60,90,-60,-30]_{2s}$  specimens.

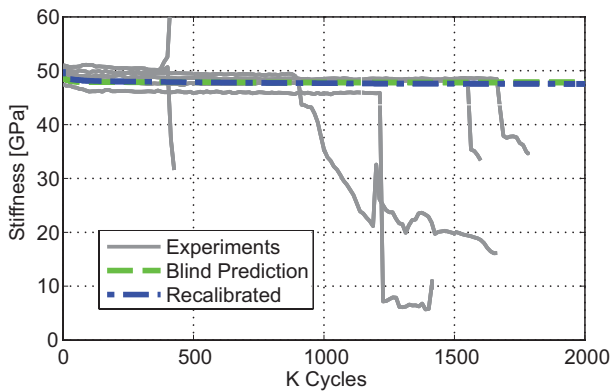


**Figure 6.** Stiffness vs. cycles for  $[0,45,90,-45]_{2s}$  layup under tension-tension fatigue.

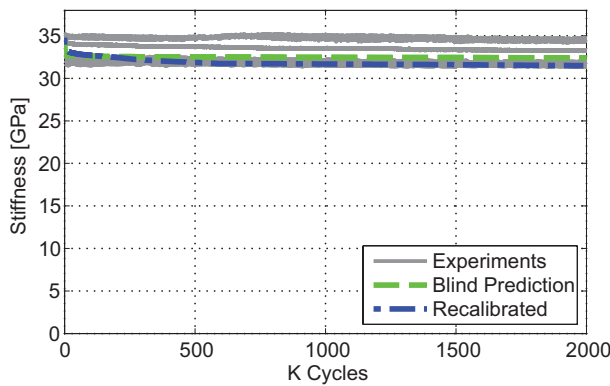


**Figure 7.** Stiffness vs. cycles for  $[30,60,90,-60,-30]_{2s}$  layup under tension-tension fatigue.

Figure 8 shows the comparison of the stiffness degradation behavior in the  $[60,0,-60]_{3s}$  specimens as simulated in the blind prediction and recalibration phases compared with the experimental observations. This layup contains the largest percentage of  $0^\circ$  plies and the applied load level is the greatest percentage of static ultimate strength (80%) of all three layups. A clear discrepancy in the stiffness degradation behavior exists between the blind prediction and the experiments. Failure of the  $[60,0,-60]_{3s}$  specimen was predicted after approximately 700 cycles, whereas experiments show a pronounced and progressive stiffness drop, yet no specimen failure, up to runout at 2 million cycles. In the experiments, each replicate displayed a gradual

stiffness degradation over time from an average stiffness of 51.2 GPa at the first cycle to 39.3 GPa after 2M cycles. This amounts to a 23% degradation of stiffness. In the recalibrated simulation, the stiffness dropped from an initial value of 51.2 GPa to 34.8 GPa over 100K cycles, where the stiffness remained at 34.8 GPa up to run out at 2M cycles. While the rate of stiffness degradation as predicted by the model remains higher than the experiments, the magnitude of the stiffness drop and the overall behavior is better captured after recalibration.

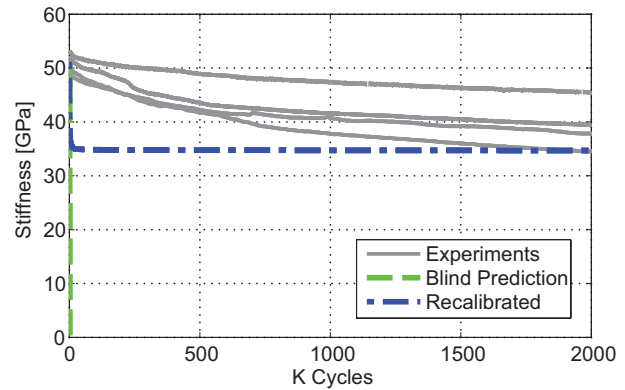


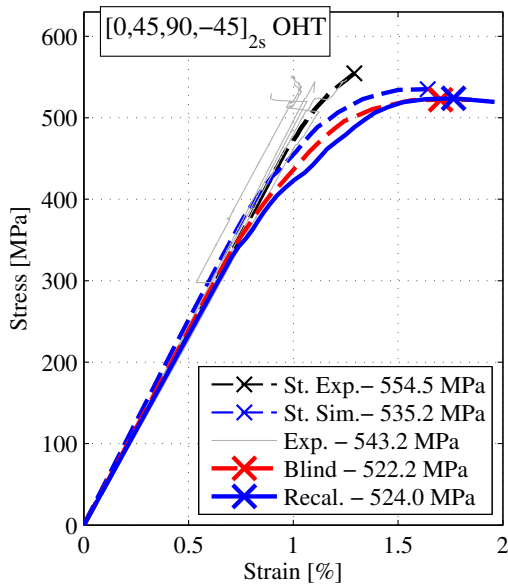
**Figure 8.** Stiffness vs. cycles for  $[60,0,-60]_{3s}$  layup under tension-tension fatigue.

### Residual Strength after Fatigue

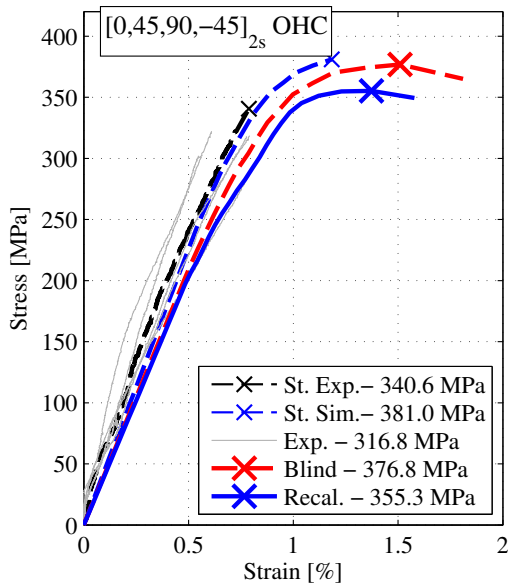
The residual strength in tension and compression after fatigue was predicted after 300K cycles for the  $[0,45,90,-45]_{2s}$  layup and after 200K cycles for the  $[30,60,90,-60,-30]_{2s}$  and  $[60,0,-60]_{3s}$  layups. In Figures 9 - 11, the experimental stress vs. strain curves of the fatigue specimens are compared to the blind and recalibrated predictions. Additionally, the experimental mean and the predicted *static* strength of virgin (i.e., unfatigued) specimens are shown for comparison.

The residual strength predictions for the  $[0,45,90,-45]_{2s}$  specimen are shown in Figure 9. The strength reduction after fatigue for the specimen subjected to tension was 2.0%, comparing the experimental mean ultimate strength of the virgin and fatigued specimens. In compression a 7.0% strength drop was observed. This behavior is well captured by the model. For the tension case there is a 2.1% drop in ultimate strength after fatigue exposure as predicted by the simulations. For compression the predicted drop is 6.7%. These values are in very good agreement with the experiments. The additional ductility predicted in the simulations compared to the experiments near ultimate strength is a result of the CDM representation of diffuse microscopic damage as a stiffness loss over the entire element containing the failing quadrature point. As the stiffness loss is not localized to distinct cracks, the simulation tends to display more ductile failure behavior as elements around the open hole begin to fail.

Figure 10 shows the residual strength predictions for the  $[30,60,90,-60,-30]_{2s}$  layups in tension and compression. The model recalibration to better account for interlaminar shear behavior significantly increased the residual strength predictions for this layup in tension and compression.



(a)

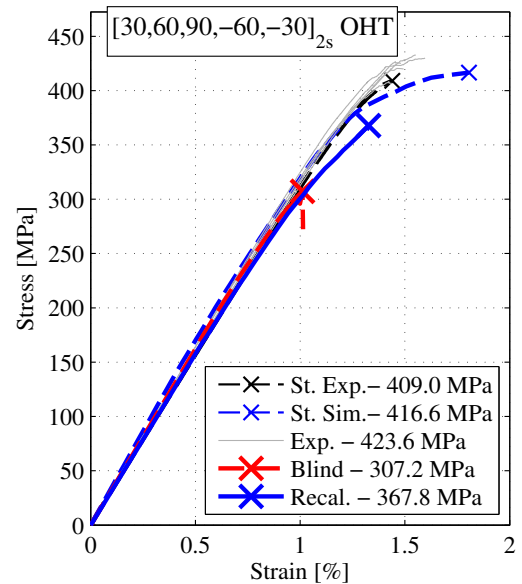


(b)

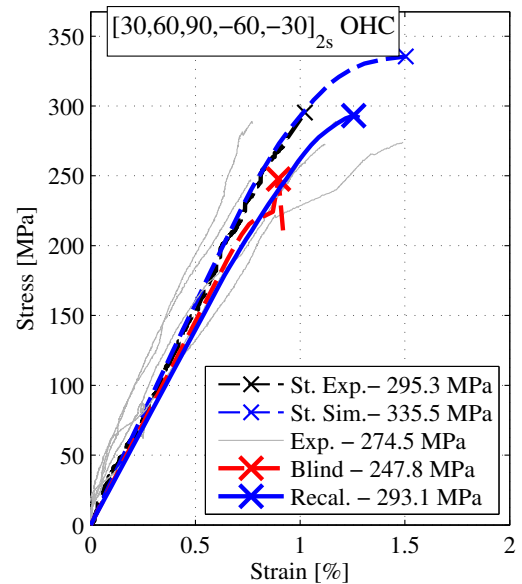
**Figure 9.** Residual strength after 300k cycles for  $[0,45,90,-45]_{2s}$  layout in (a) tension and (b) compression.

In tension experiments, a 3.6% increase in strength for fatigued specimens compared to the static ultimate strength of virgin specimens was observed. In contrast, the residual compression strength was 7.0% lower than the static ultimate strength of the virgin specimen in compression. In tension and compression loading, the recalibrated model predicts a drop of 11.7% and 12.6% for tension and compression residual strength, respectively.

No blind prediction of residual strength was made for the  $[60,0,-60]_{3s}$  layout due to the early failure of the simulation under fatigue. The recalibrated model predictions of residual strength were in reasonable agreement with the experiments as shown in Figure 11. A 24.4% increase in residual strength in tension after fatigue compared to the static ultimate strength was observed in the experiments. This is because of load redistributions caused by fiber splitting and stress



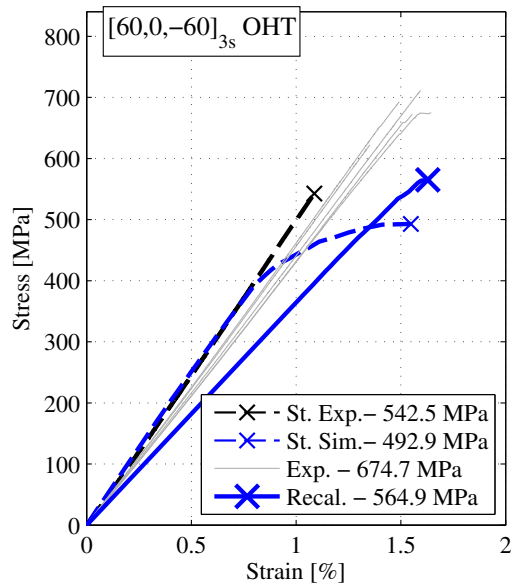
(a)



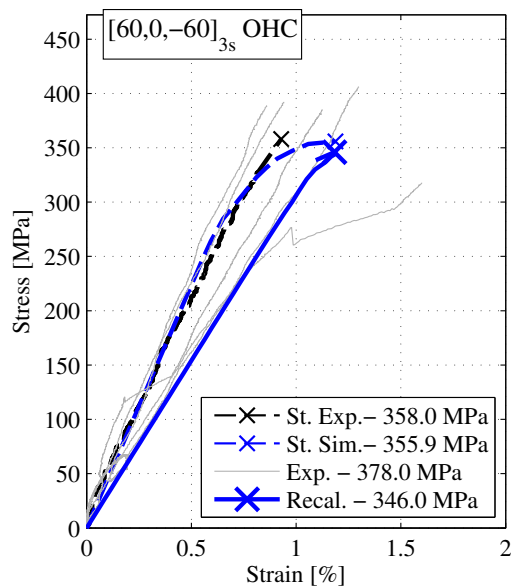
(b)

**Figure 10.** Residual strength after 200k cycles for  $[30,60,90,-60,-30]_{2s}$  layout in (a) tension and (b) compression.

shielding around the hole. The recalibrated model captured the general trend of this behavior as well, predicting a strength increase of 14.6% in tension. The effect of the rapid stiffness drop in the simulation of this layout from fatigue is evident in Figure 11(a), leading to the stiffness discrepancy between experiments and the simulation. In compression, the experiments show a 5.6% increase in strength after fatigue. This is not captured in the simulation, where a 2.8% drop in strength is predicted. In both residual strength predictions of this layout, the high degree of nonlinearity in the stress-strain curve that is observed in the static results is not present.



(a)



(b)

**Figure 11.** Residual strength after 200k cycles for  $[60,0,-60]_{3s}$  layup in (a) tension and (b) compression.

### Damage Contour Plots

Damage contour plots from the prediction of damage accumulation in the fatigue simulations and the X-ray CT images of experimental damage are provided to compare the characteristics of damage accumulation between the experiments and the prediction model. Figures 12 and 13 show the ply-by-ply damage accumulation corresponding to fiber failure, transverse matrix cracking, and delamination from the recalibrated fatigue simulation alongside the experimental CT images displaying damage in the experiments for the  $[0,45,90,-45]_{2s}$  layup after 100K and 300K fatigue cycles, respectively. The damage pattern is consistent between the simulations and the experiments. In the  $0^\circ$  plies, the growth of a small region of fiber splitting due to transverse matrix damage is seen in both

the experiments and predictions. The major damage mode of transverse matrix cracking in the fiber direction of the  $\pm 45^\circ$  plies is captured in the simulations. The fatigue loading rapidly leads to transverse matrix cracks over nearly the full width of the specimen in the  $+45^\circ$  and  $-45^\circ$  plies, with the cracks growing with additional cycles in both the simulations and the experiments. Matrix cracks are also present in the  $90^\circ$  plies near the hole. The predicted matrix damage in the  $90^\circ$  plies was less than that observed in the experiments. There is also evidence of delamination around the hole in the interior  $0^\circ$  ply which is predicted in the simulations, but significant delamination regions near the fiber splitting are not observed in the simulations, particularly due to the relatively coarse mesh used in the analyses. Damage accumulation in the  $[30,60,90,-60,-30]_{2s}$  layup was predicted to occur predominantly in the  $\pm 60^\circ$  plies as seen in Figures 14 and 15. The damage extent predicted in the  $\pm 60^\circ$  plies is larger than that observed in the CT images of the same plies. An additional major damage mode observed in the experiments was a transverse matrix crack in the  $\pm 30^\circ$  plies, which was predicted well in the simulation. In the damage contours shown below, the general cross pattern of damage in the  $30^\circ$  plies is predicted in the recalibrated simulations, but appears to be accumulating faster than in the experiments, as the CT images indicate. A large number of short transverse matrix cracks are observed in the CT images near the primary cracks in the  $\pm 30^\circ$  plies. Delamination is not dominant in the predicted contours, but delaminated regions are evident in the experimental images around the major cracks in the  $\pm 30^\circ$  directions. There is no fiber failure predicted or observed in this layup.

The recalibrated prediction of damage accumulation in the  $[60,0,-60]_{3s}$  layup is in good qualitative agreement with the experiments in Figure 16, but progresses more rapidly than in the experiments. The simulation displays more delaminations than the CT images display, but the general pattern of the delamination in the  $0^\circ$  plies extending above and below the hole in the loading direction agrees well with the experiments. Additionally, the fiber splitting from transverse matrix damage on either side of the delamination region is well captured. The predominance of transverse matrix cracking is seen in the simulations and in the experiments with a large number of matrix cracks across the width of the specimen, as well as near complete transverse matrix damage in the simulated  $\pm 60^\circ$  plies. Fiber failure in the predictions is limited to the delamination region, with no fiber failure propagating transverse to the loading direction away from the hole. The premature prediction of such extensive damage is consistent with the rapid stiffness reduction observed in the stiffness vs. life curve of this specimen in Figure 8.

### Conclusion

This investigation detailed the predictive capability of the reduced order space-time homogenization method in predicting the fatigue failure behavior of laminated composite specimens. In blind predictions, the model was able to capture the progressive stiffness degradation behavior, damage distribution across the specimens, as well as the residual strength for the  $[0,45,90,-45]_{2s}$  and

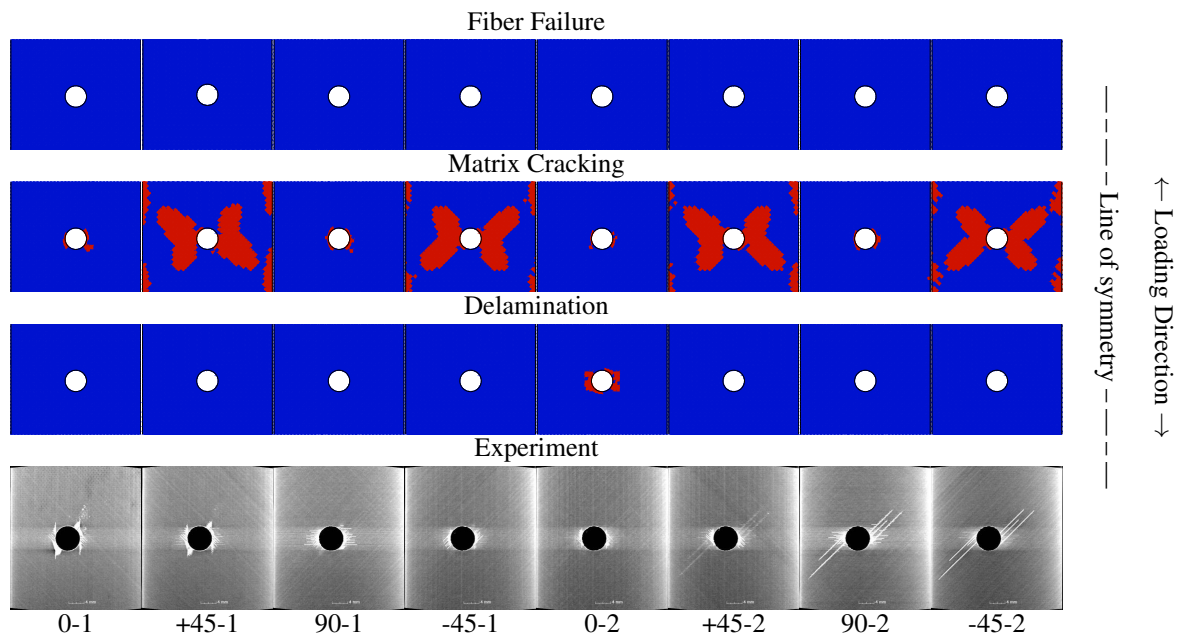


**Figure 12.** Fatigue damage contours for  $[0,45,90,-45]_{2s}$  layup after 100k cycles.

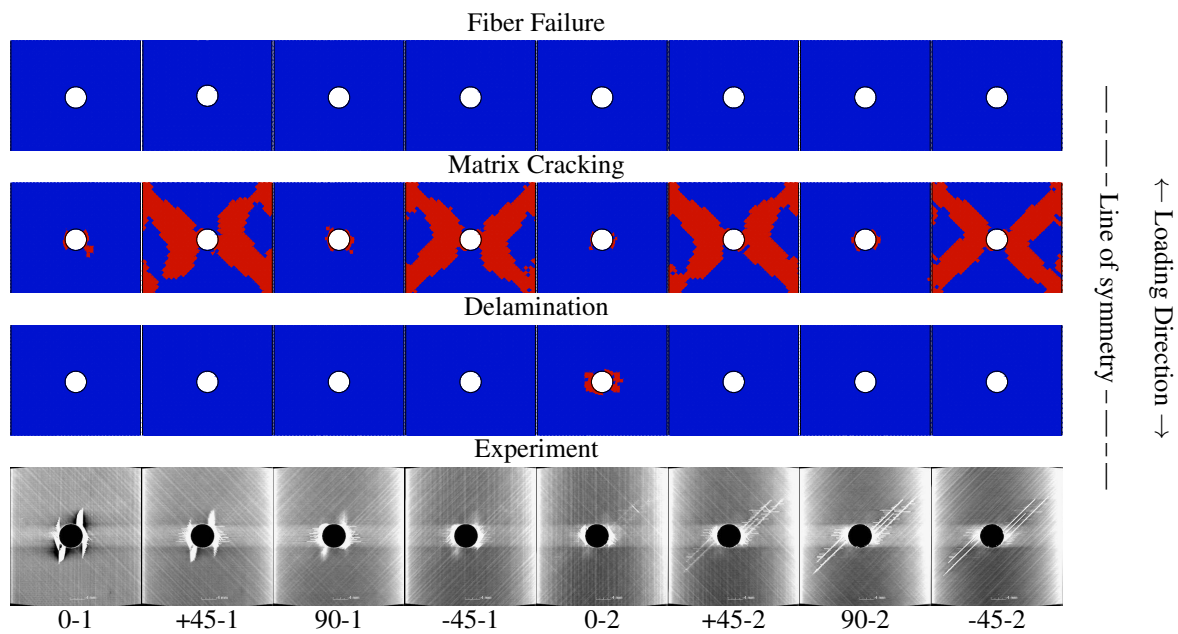


**Figure 13.** Fatigue damage contours for  $[0,45,90,-45]_{2s}$  layup after 300k cycles.

$[30,60,90,-60,-30]_{2s}$  layups in a reasonably accurate fashion. After recalibrating the model to account for delamination behavior using the end notch flexure test data, the prediction of the fatigue behavior of the  $[60,0,-60]_{3s}$  layup was also in good qualitative agreement with the experiments.

By this study, we observed the significant role of shear delamination on the overall failure characteristics in the  $[60,0,-60]_{3s}$  layup. We note that the same failure mechanism did not have as prominent a role for the  $[0,45,90,-45]_{2s}$  and  $[30,60,90,-60,-30]_{2s}$  layups. These results point to the effect of the interaction of damage modes and the sensitivity of these interactions on the composite layup and potentially the structural configuration of the composite. The interactions between various failure mechanisms under

different composite configurations and the ability of progressive damage models in predicting these interactions will therefore be subject to further investigations.

## Acknowledgments

The authors gratefully acknowledge the financial support provided by the Aerospace Systems Directorate of the Air Force Research Laboratory (Contract No: GS04T09DBC0017 through Engility Corporation) and the Department of Defense (DoD) through the National Defense Science & Engineering Graduate Fellowship (NDSEG) Program.

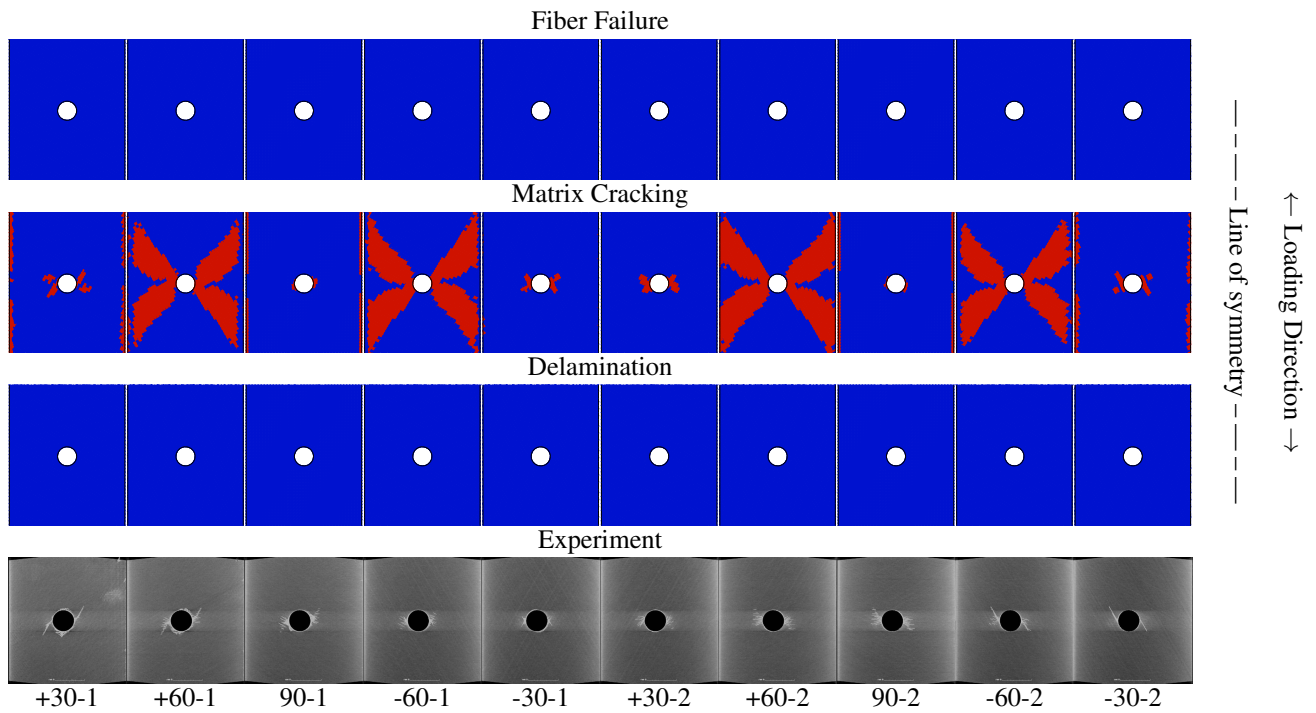


**Figure 14.** Fatigue damage contours for  $[30,60,90,-60,-30]_{2s}$  layup after 50k cycles.

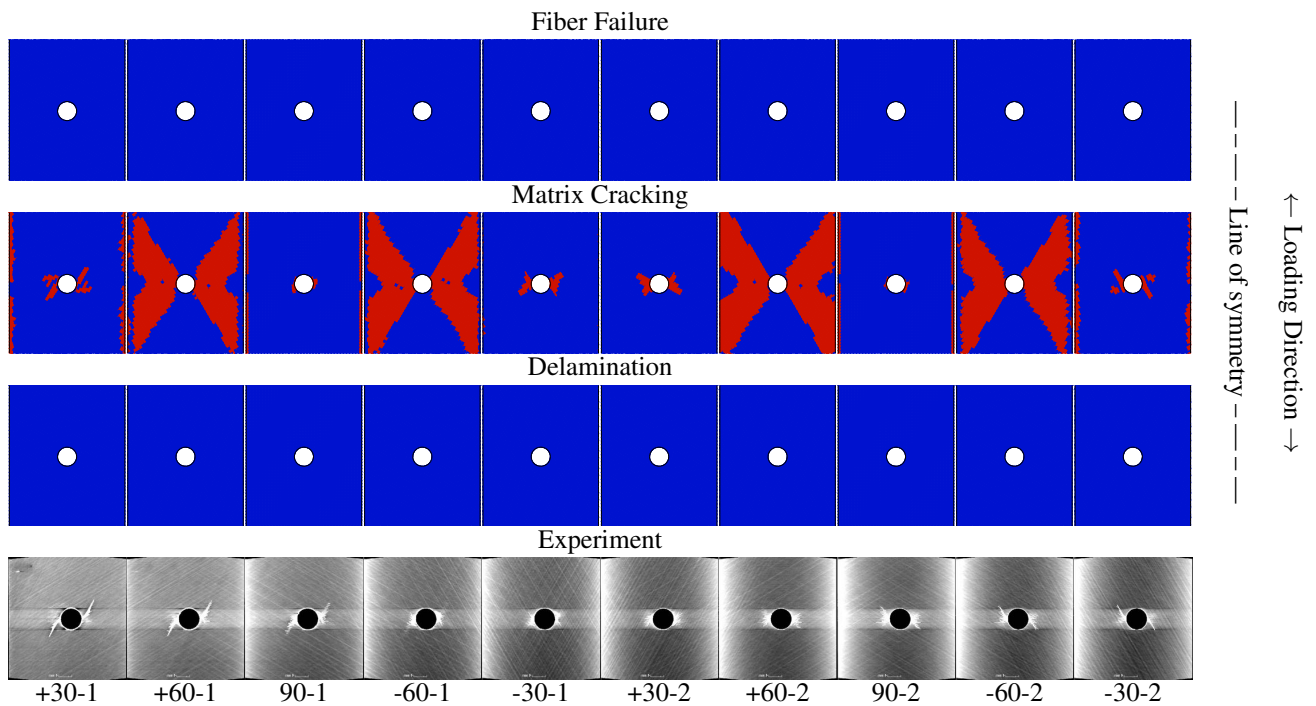


**Figure 15.** Fatigue damage contours for  $[30,60,90,-60,-30]_{2s}$  layup after 200k cycles.

## References

- G. F. Abdelal, A. Caceres, and E. J. Barbero. A micro-mechanics damage approach for fatigue of composite materials. *Compos. Struct.*, 56:413–422, 2002.
- J. Aboudi. A continuum theory for fiber-reinforced elastic-viscoplastic composites. *Int. J. Eng. Sci.*, 20:605–621, 1982.
- D. H. Allen, C. E. Harris, and S. E. Groves. A thermomechanical constitutive theory for elastic composites with distributed damage—i. theoretical development. *Int. J. Solids Struct.*, 23: 1301–1318, 1987.
- M. Anahid, P. Chakraborty, D. S. Joseph, and S. Ghosh. Wavelet decomposed dual-time scale crystal plasticity fe model for analyzing cyclic deformation induced crack nucleation in polycrystals. *Modell. Simul. Mater. Sci. Eng.*, 17:064009, 2009.
- M. J. Bogdanor and C. Oskay. Prediction of progressive damage and strength of IM7/977-3 composites using the eigendeformation based homogenization approach: Static loading. *J. Compos. Mater.*, in review, 2016.

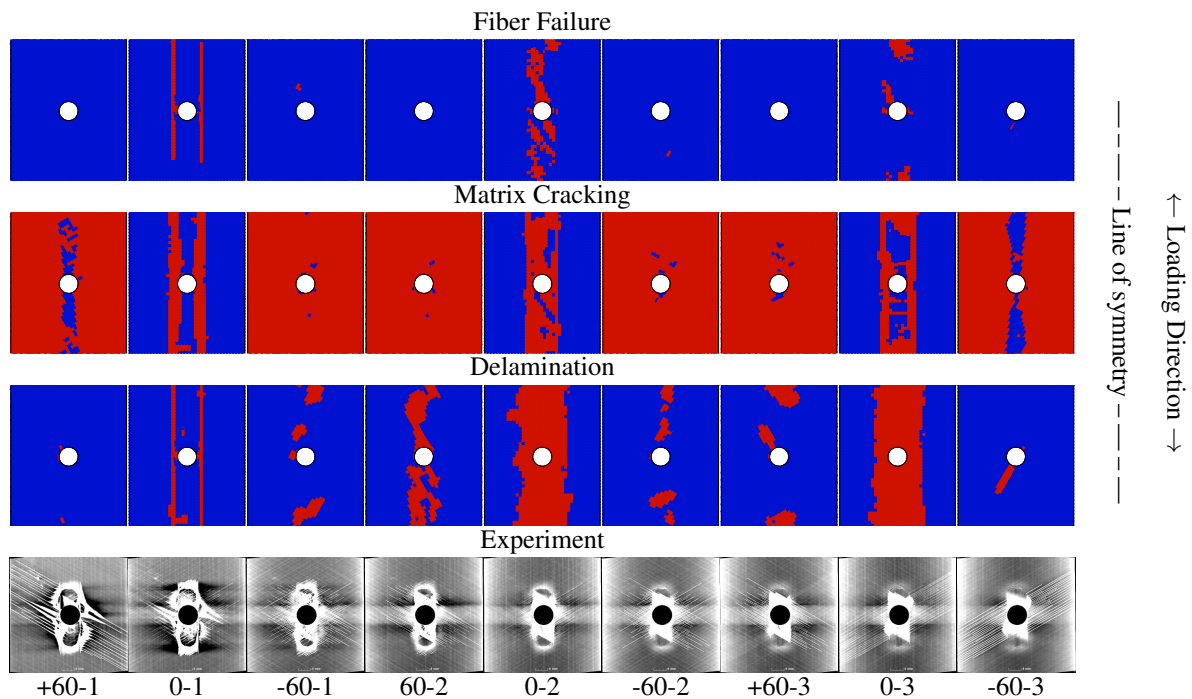


**Figure 16.** Fatigue damage contours for  $[60,0,-60]_{3s}$  layup after 200k cycles.

- M. J. Bogdanor, S. Mahadevan, and C. Oskay. Uncertainty quantification in damage modeling of heterogeneous materials. *Int. J. Multiscale Comp. Eng.*, 11:287–307, 2013.
- M. J. Bogdanor, C. Oskay, and S. B. Clay. Multiscale modeling of failure in composites under model parameter uncertainty. *Comput. Mech.*, 56:389–404, 2015.
- P. P. Camanho, P. Maimí, and C. G. Dávila. Prediction of size effects in notched laminates using continuum damage mechanics. *Compos. Sci. Technol.*, 67:2715–2727, 2007.
- P. P. Castañeda. The effective mechanical properties of nonlinear isotropic composites. *J. Mech. Phys. Solids*, 39:45–71, 1991.
- R. D. Crouch and C. Oskay. Symmetric mesomechanical model for failure analysis of heterogeneous materials. *Int. J. Multiscale Comp. Eng.*, 8:447–461, 2010.
- R. D. Crouch and C. Oskay. Accelerated time integrator for multiple time scale homogenization. *Int. J. Numer. Meth. Eng.*, 101:1019–1042, 2015.
- R. D. Crouch, C. Oskay, and S. Clay. Multiple spatio-temporal scale modeling of composites subjected to cyclic loading. *Comput. Mech.*, 48:59–67, 2013.
- G. J. Dvorak. Transformation field analysis of inelastic composite materials. *Proc. Roy. Soc. London Ser. A*, 437:311–327, 1992.
- J. Fish. *Practical multiscale modeling*. John Wiley & Sons, 2013.
- J. Fish and Q. Yu. Multiscale damage modelling for composite materials: Theory and computational framework. *Int. J. Numer. Meth. Eng.*, 52:161–191, 2001.
- J. Fish and Q. Yu. Computational mechanics of fatigue and life predictions for composite materials and structures. *Comput. Meth. Appl. Mech. Eng.*, 191:4827–4849, 2002.
- J. Fish and Z. Yuan. Multiscale enrichment based on partition of unity. *Int. J. Numer. Meth. Eng.*, 62:1341–1359, 2005.
- J. Fish, K. Shek, M. Pandheeradi, and M. S. Shephard. Computational plasticity for composite structures based on mathematical homogenization: Theory and practice. *Comput. Meth. Appl. Mech. Eng.*, 148:53–73, 1997.
- E. K. Gamstedt and S. Ostlund. Fatigue propagation of fibre-bridged cracks in unidirectional polymer-matrix composites. *Appl. Comp. Mater.*, 8:385–410, 2001.
- S. Ghosh and S. Moorthy. Elastic-plastic analysis of arbitrary heterogeneous materials with the voronoi-cell finite-element method. *Comput. Meth. Appl. Mech. Eng.*, 121:373–409, 1995.
- P. W. Harper and S. R. Hallett. A fatigue degradation law for cohesive interface elements—development and application to composite materials. *Int. J. Fatigue*, 32:1774–1787, 2010.
- Z. Hashin and A. Rotem. A fatigue failure criterion for fiber reinforced materials. *J. Compos. Mater.*, 7:448–464, 1973.
- J. A. Hernández, J. Oliver, A. E. Huespe, M. A. Caicedo, and J. C. Cante. High-performance model reduction techniques in computational multiscale homogenization. *Comput. Meth. Appl. Mech. Eng.*, 276:149–189, 2014.
- T. Y. Hou and X.-H. Wu. A multiscale finite element method for elliptic problems in composite materials and porous media. *J. Comput. Phys.*, 134:169–189, 1997.
- L. Kachanov. *Introduction to continuum damage mechanics*, volume 10. Springer Science & Business Media, 2013.
- V. G. Kouznetsova. *Computational Homogenization for the multi-scale Analysis of multi-phase materials*. PhD thesis, Technische Universiteit Eindhoven, 2002.
- P. Ladeveze and E. LeDantec. Damage modelling of the elementary ply for laminated composites. *Compos. Sci. Technol.*, 43:257–267, 1992.
- C. S. Lee and W. Hwang. Fatigue life prediction of matrix dominated polymer composite materials. *Polym. Compos.*, 21:798–805, 2000.
- J. Lemaitre. *A course on damage mechanics*. Springer Science & Business Media, 2012.
- A. Matzenmiller, J. Lubliner, and R. L. Taylor. A constitutive model for anisotropic damage in fiber-composites. *Mech. Mater.*, 20:

- 125–152, 1995.
- C. Miehe, J. Schröder, and J. Schotte. Computational homogenization analysis in finite plasticity simulation of texture development in polycrystalline materials. *Comput. Meth. Appl. Mech. Eng.*, 171:387–418, 1999.
- H. Moulinec and P. Suquet. A fast numerical-method for computing the linear and nonlinear mechanical-properties of composites. *Cr. Acad. Sci. II*, 318:1417–1423, 1994.
- J. A. Nelder and R. Mead. A simplex method for function minimization. *Comput. J.*, 7:308–313, 1965.
- C. Oskay. Variational multiscale enrichment for modeling coupled mechano-diffusion problems. *Int. J. Numer. Meth. Eng.*, 89: 686–705, 2012.
- C. Oskay. *Numerical Modelling of Failure in Advanced Composite Materials*, chapter Multiscale Modeling of the Response and Life Prediction of Composite Materials. Woodhead publishing, 2015.
- C. Oskay and J. Fish. Fatigue life prediction using 2-scale temporal asymptotic homogenization. *Int. J. Numer. Meth. Eng.*, 61:329–359, 2004a.
- C. Oskay and J. Fish. Multiscale modeling of fatigue for ductile materials. *Int. J. Multiscale Comp. Eng.*, 2:329–353, 2004b.
- C. Oskay and J. Fish. Eigendeformation-based reduced order homogenization for failure analysis of heterogeneous materials. *Comput. Meth. Appl. Mech. Eng.*, 196:1216–1243, 2007.
- M. H. J. W. Paas, P. J. G. Schreurs, and W. A. M. Brekelmans. A continuum approach to brittle and fatigue damage: Theory and numerical procedures. *Int. J. Solids. Struct.*, 30:579–599, 1993.
- P. C. Paris and F. Erdogan. A critical analysis of crack propagation laws. *J. Basic Eng.*, 85:528–533, 1963.
- J. Payan and C. Hochard. Damage modelling of laminated carbon/epoxy composites under static and fatigue loadings. *Int. J. Fatigue*, 24:299–306, 2002.
- M.-J. Pindera and B. A. Bednarczyk. An efficient implementation of the generalized method of cells for unidirectional, multi-phased composites with complex microstructures. *Compos. Part B-Eng.*, 30:87–105, 1999.
- A. Poursartip, M. F. Ashby, and P. W. R. Beaumont. The fatigue damage mechanics of a carbon fibre composite laminate: I–development of the model. *Compos. Sci. Technol.*, 25:193–218, 1986.
- K. L. Reifsnider and A. Talug. Analysis of fatigue damage in composite laminates. *Int. J. Fatigue*, 2:3–10, 1980.
- A. J. Russell and K. N. Street. The effect of matrix toughness on delamination: static and fatigue fracture under mode II shear loading of graphite fiber composites. *Toughened Composites, ASTM STP*, 937:275–294, 1987.
- S. M. Spearing, P. W. R. Beaumont, and M. F. Ashby. Fatigue damage mechanics of composite materials. II: A damage growth model. *Compos. Sci. Technol.*, 44:169–177, 1992.
- K. Terada and N. Kikuchi. Nonlinear homogenization method for practical applications. In S. Ghosh and M. Ostoja-Starzewski, editors, *Computational Methods in Micromechanics*, volume AMD-212/MD-62, pages 1–16. ASME, 1995.
- A. Turon, P. P. Camanho, J. Costa, and C. G. Davila. A damage model for the simulation of delamination in advanced composites under variable-mode loading. *Mech. Mater.*, 38: 1072–1089, 2006.
- E. Weinan and B. Engquist. The heterogenous multiscale methods. *Commun. Math. Sci.*, 1:87–132, 2003.
- J. Yvonnet and Q.-C. He. The reduced model multiscale method (R3M) for the non-linear homogenization of hyperelastic media at finite strains. *J. Comput. Phys.*, 223:341–368, 2007.